

MAX-PLANCK-INSTITUT FÜR PLASMAPHYSIK
GARCHING BEI MÜNCHEN

3D Collisional Drift-Wave Turbulence,
Role of Magnetic Shear

A. Zeiler, D. Biskamp and J.F. Drake

IPP 6/339

February 1996

*Die nachstehende Arbeit wurde im Rahmen des Vertrages zwischen dem
Max-Planck-Institut für Plasmaphysik und der Europäischen Atomgemeinschaft über die
Zusammenarbeit auf dem Gebiete der Plasmaphysik durchgeführt.*

3D collisional Drift-Wave Turbulence, Role of Magnetic Shear

A. Zeiler, D. Biskamp, and J. F. Drake*
Max-Planck-Institut für Plasmaphysik,
EURATOM Association, 85748 Garching, Germany

Abstract

We present three-dimensional (3D) nonlinear simulations of collisional drift-wave turbulence. Results for the Hasegawa-Wakatani equations (without magnetic shear) in 3D are compared to former two-dimensional (2D) simulations. In contrast to the 2D system the 3D situation is completely dominated by a nonlinear drive mechanism. The final state of the system is sensitive to the configuration of the computational grid since the sheared flow develops at the longest scales of the system. When magnetic shear is included, the system is linearly stable but the turbulence self-sustains by basically the same nonlinear mechanism. Magnetic shear limits the size of the dominant eddies, so the system evolves to a stationary turbulent state independent of the computational box. Finally, we show that the level of turbulence in the system with magnetic shear depends sensitively on the size of the effective Larmor radius ρ_s compared with the characteristic transverse scale length of the eddies.

*Institute for Plasma Research, University of Maryland, College Park, Maryland, 20742, USA

1 Introduction

The large energy and particle losses observed in magnetically confined plasmas are now generally attributed to small-scale electrostatic fluctuations. In the cool collisional plasma edge these fluctuations are described by resistive drift wave models. A particularly simple drift-wave model is that due to Hasegawa-Wakatani [1] which neglects all effects of the magnetic geometry considering only the two fluctuating quantities, density and potential, in a straight magnetic field. Since this model still requires simulations in three-dimensional (3D) space, it is usually further reduced to a two-dimensional (2D) system, which has been widely investigated by several groups [2][3]. In particular the high resolution simulations of ref. [3] yield stationary turbulence, which for sufficiently high Reynolds number is independent of the damping coefficients. The inclusion of magnetic shear stabilizes the linearized equations. Decaying turbulence in the resulting 2D system was studied by Scott [4].

In the following work we present 3D simulations in unsheared and sheared magnetic geometry. Effects due to magnetic curvature are neglected here but are reported elsewhere (refs. [5] and [6]). The equations are introduced and briefly discussed in section 2, while section 3 gives an outline of the numerical methods. In section 4, we show the results of simulations in the unsheared system. The most important finding is the existence of a nonlinear drive which leads to a bursty behavior with maximum transport levels greatly exceeding that in the 2D system. The turbulence continuously grows until a strong poloidal shear-flow develops and completely suppresses the turbulence. In section 5 we discuss the 3D system in sheared magnetic field. Although the system is linearly stable, the nonlinear mechanism identified in the unsheared case maintains the system in a self-sustained turbulent state. The fluctuation level and the transport strongly depend on the ratio of the Larmor radius to the characteristic transverse eddy scale length, which is controlled by the magnetic shear.

2 Equations

Since the detailed derivation of the nonlinear equations is reported elsewhere [1][5][6], we only give a brief summary. The equations consist of the continuity equation

$$\frac{dn}{dt} - \nabla \cdot \left(\frac{nc}{\Omega_i B} \frac{d}{dt} \nabla_{\perp} \phi \right) = 0 \quad (1)$$

and the vorticity equation

$$\nabla \cdot \left(\frac{nc}{\Omega_i B} \frac{d}{dt} \nabla_{\perp} \phi \right) - \nabla_{\parallel} \frac{j_{\parallel}}{e} = 0, \quad (2)$$

where $d/dt = \partial/\partial t + \vec{v}_{\perp}^0 \cdot \nabla$, $\vec{v}_{\perp}^0 = -c \nabla \phi \times \vec{B}/B^2$ and $\eta j_{\parallel} = -\nabla \phi + (T_e/e) \nabla_{\parallel} \ln n$ and \parallel and \perp indicate directions parallel and perpendicular to the local magnetic field,

$\vec{B} = B_0[\vec{z} - (x/L_s)\vec{y}]$, L_s being the magnetic shear length. The ions are assumed to be cold and the electron temperature is kept constant. The first term in the continuity equation describes the change of density due to $\vec{E} \times \vec{B}$ convection and the second term arises from the divergence of the ion polarization drift. The vorticity equation balances currents due to ion and electron motion. The first term again arises from the divergence of the ion polarization drift. Charge neutrality is maintained by a parallel current which is connected to density and potential by Ohm's law.

To improve spatial resolution in the case of a sheared magnetic field we transform to a twisted slab coordinate system with z -aligned magnetic field lines [6]. Splitting the density into profile n_0 and fluctuation \tilde{n} components and using the normalizations

$$x \sim L_\perp, y \sim L_\perp, z \sim L_\parallel, t \sim (L_n/c_s)(L_\perp/\rho_s), \quad (3)$$

$$\tilde{n} \sim n_0 L_\perp / L_n, \phi \sim (T_e/e)(L_\perp / L_n),$$

with L_\parallel not yet specified and the perpendicular scale length given by

$$L_\perp = \left(\frac{\rho_s^2 L_\parallel^2 \nu_{ei}}{2\Omega_e L_n} \right)^{1/3}, \quad (4)$$

($\rho_s = c_s/\Omega_i$, $c_s^2 = T_e/m_i$) the drift-wave equations are given by

$$\frac{d}{dt} \nabla_\perp^2 \phi + \frac{\partial^2}{\partial z^2} (\phi - n) = D^\phi, \quad (5)$$

$$\frac{dn}{dt} + \frac{\partial \phi}{\partial y} + \hat{\rho}_s^2 \frac{\partial^2}{\partial z^2} (\phi - n) = D^n, \quad (6)$$

with $\hat{\rho}_s = \rho_s / L_\perp$,

$$\frac{d}{dt} = \frac{\partial}{\partial t} - (\nabla_\perp \phi \times \vec{z}) \cdot \nabla_\perp, \quad \nabla_\perp^2 = \left(\frac{\partial}{\partial x} + z \frac{L_\parallel}{L_s} \frac{\partial}{\partial y} \right)^2 + \frac{\partial^2}{\partial y^2}. \quad (7)$$

The viscosity operators D^n and D^ϕ will be specified later. Multiplying eq. (5) by ϕ and eq. (6) by n and integrating over all space leads to the total rate of change of the turbulent energy

$$\frac{d}{dt} \frac{1}{2} \int \left((\nabla_\perp \phi)^2 + \frac{n^2}{\hat{\rho}_s^2} \right) d^3x = - \int \left(\frac{n}{\hat{\rho}_s^2} \frac{\partial \phi}{\partial y} + \left[\frac{\partial}{\partial z} (\phi - n) \right]^2 + \phi D^\phi - \frac{n}{\hat{\rho}_s^2} D^n \right) d^3x. \quad (8)$$

The turbulent transport is given by

$$\Gamma = \langle n v_{rad} \rangle = - \langle n \frac{\partial \phi}{\partial y} \rangle \quad (9)$$

with $\langle \dots \rangle$ denoting an average over all space. As a consequence of the normalization given in eqs. (3) and (4), the anomalous diffusion coefficient formally obeys the scaling

$$D_{an} = D_0 \Gamma, \quad D_0 = \frac{cT_e}{eB} \frac{L_\perp}{L_n}. \quad (10)$$

In the presence of magnetic shear the natural parallel scale length is simply $L_\parallel = 2\pi L_s$ so that ∇_\perp^2 simplifies to

$$\nabla_\perp^2 = \left(\frac{\partial}{\partial x} + 2\pi z \frac{\partial}{\partial y} \right)^2 + \frac{\partial^2}{\partial y^2}.$$

The coupling of parallel and perpendicular dynamics transforms this parallel scale length to the natural transverse scale length L_\perp defined in eq. (4). A second transverse scale length is ρ_s , the effective Larmor radius. The drift-wave equations with magnetic shear therefore depend on the parameter $\hat{\rho}_s$, the ratio of these two scale lengths. In the absence of magnetic shear ρ_s is the only transverse scale so that we can choose $L_\perp = \rho_s$ to define the natural parallel scale length,

$$L_\parallel = \left(\frac{2L_n T_e}{c_s m_e \nu_{ei}} \right)^{1/2},$$

which is obtained by solving eq. (4) for L_\parallel . In this normalization the anomalous diffusion coefficient (eq. 10) obeys the usual Gyro-Bohm scaling,

$$D_{an} = D_{GB} \Gamma, \quad D_{GB} = \frac{cT_e}{eB} \frac{\rho_s}{L_n},$$

and ∇_\perp^2 in eq. (7) reduces to the standard form in the absence of magnetic shear, $L_s \rightarrow \infty$. $\hat{\rho}_s$ in eqs. (6) and (8) is replaced by unity. The resulting equations were first derived by Hasegawa and Wakatani [1].

3 Numerical Methods

For the numerical simulations two different schemes were used. In the unsheared geometry periodic boundary conditions may be applied in all three dimensions. Therefore we transform all quantities into k -space and use a pseudo-spectral approach (see also ref. [7]). The nonlinearities are evaluated in real space with dealiasing according to the 2/3 rule and incorporated into the time stepper according to an Adams-Bashforth scheme. The viscosities are computed exactly, allowing high order diffusion operators without any stability or accuracy constraints. The remaining linear terms are solved implicitly to maintain numerical stability which is of particular importance for the parallel diffusions terms $\nabla_\parallel^2(\phi - n)$. The energy equation (8) is used to check the accuracy of the time-stepping scheme.

The sheared case is more complicated: The operator ∇_{\perp}^2 (eq. 7) contains the variable z , which breaks the periodicity in the z direction and prohibits the Fourier representation in this direction. Furthermore the larger the value of z in this operator the more modes are required to resolve the relevant structures. To circumvent this problem we split the computational domain into several boxes in the parallel direction and relate z to the center of the local box. Within each box n and ϕ are advanced implicitly in real space and afterwards the boxes are explicitly matched together leading to a quasi-periodic system in parallel direction. The numerical scheme including the matching procedure is described in detail in ref. [6], hence we repeat here only the main features. In the perpendicular plane we Fourier transform n and ϕ using periodic boundary conditions, which avoid profile flattening effects and allow us to follow the system into a stationary state. The nonlinearities are evaluated in real space, in most simulations with dealiasing. To advance n and ϕ in time the nonlinearities are implemented according to a leapfrog algorithm. The diffusion operators are solved exactly and all remaining (linear) terms are solved implicitly using a block tridiagonal solver for the z -direction.

4 Simulations without Magnetic Shear

4.1 2D Test Run

In the unsheared case we solve eqs. (5) and (6) with the modifications described previously. The linear properties of this system are well known (in particular the fact that it is linearly unstable); a detailed discussion may be found in ref. [3]. To cut the spectrum at high mode numbers we use the hyperviscosities $D^n = \nu \nabla_{\perp}^6 n$ and $D^{\phi} = \nu \nabla_{\perp}^8 \phi$. For reference we apply our code to the well studied 2D problem, which is obtained by replacing the operator $-\partial^2/\partial z^2$ by a constant C called the adiabaticity parameter. This means the parallel dissipation terms are evaluated at a fixed $k_z \neq 0$. Note however that for the nonlinearities we assume $k_z = 0$ since there is no direct nonlinear interaction between modes with the same $k_z \neq 0$. Thus, these equations do not model any physical system. The equations

$$\frac{dn}{dt} + \frac{\partial \phi}{\partial y} - C(\phi - n) = \nu \nabla_{\perp}^6 n, \quad (11)$$

$$\frac{d}{dt} \nabla_{\perp}^2 \phi - C(\phi - n) = \nu \nabla_{\perp}^8 \phi \quad (12)$$

are solved with the box dimensions $L_x = L_y = 36$, the mode numbers $N_x = N_y = 48$ (complex modes corresponding to 96 collocation points) and the viscosity parameter $\nu = 10^{-4}$. In Table 1 we list the average saturation levels of energy density and turbulent flux for $C = 0.1$, $C = 1$, and $C = 5$. The agreement with the values reported in refs. [2] and [3] is good in particular if the different viscosities and the lower resolution are taken into account.

C	0.1	1	5
$E/(L_x L_y)$	17.9 ± 2.8	6.1 ± 0.5	12.6 ± 0.8
Γ	2.1 ± 0.4	0.8 ± 0.1	0.18 ± 0.03

Table 1: results of 2D simulations

4.2 3D Simulation Results

The 3D simulations without magnetic shear are based directly on eqs. (5) and (6), again with modifications as discussed previously. We use the same hyperviscosities as for the 2D test case. Our reference run was performed with the box dimensions $L_x = L_y = 36$, $L_z = 38$, the mode numbers $N_x = N_y = 48$, $N_z = 24$, and the dissipation constant $\nu = 10^{-4}$. This spectrum of k_z modes corresponds to a lowest non zero C of 0.03 and a maximum of 4. The time evolution of the space averaged energy density and the space averaged flux are shown in Fig. 1.

The linear phase for $t \leq 70$ corresponds to a set of several 2D runs with C values according to the different k_z -planes, since the nonlinear interaction is negligible during this phase and the modes may be considered independent. In the subsequent initial nonlinear phase the fluctuations continue to grow. For $t \leq 230$ the energy and transport levels are still of an order of magnitude that allows an interpretation as the sum of the different 2D C -contributions. This is also seen in the plots of n and ϕ in Fig. 2. At $t = 154$ n and ϕ show a lot of small scale structure in z , which is consistent with linear theory which predicts that the growth rate peaks at high k_z for the parameters of the present simulations. The pattern in the plane perpendicular to the magnetic field is also comparable to the plots obtained in 2D [3]. If we further proceed in time, large eddies are formed in ϕ with $k_z = 0$ as the dominant mode. According to eqs. (5) and (6) the vorticity $\nabla_{\perp}^2 \phi$ is not influenced by n in this hydrodynamic situation, hence the density is convected passively by the flow. The flow itself shows the characteristics of the Euler equation. In particular the $k_z = 0$ eddies are unstable to generation of a shear-flow following the vortex peeling mechanism described in ref. [8]. This eventually leads to a radial shear flow as seen at $t = 245$ in Fig. 2. Since this flow directly extracts energy from the background density profile, we simultaneously observe a large burst of energy and transport, exceeding the value expected from the 2D runs by at least one order of magnitude. These bursts occur several times, increasing the energy stored in the turbulent eddies (see Fig. 3 at $t = 286$), until there is a rapid development of poloidal shear-flow ($t = 361$), again following the vortex peeling mechanism. In this phase the flow energy is mostly stored in $k_z = 0$ modes convecting the density only as a passive scalar. The instability mechanisms are completely suppressed leading to approximately zero transport. In ref. [7] we extended the equations to model magnetic pumping as a damping mechanism for the poloidal shear-flow. This leads to an intermittent behavior where turbulent and shear-flow states alternate.

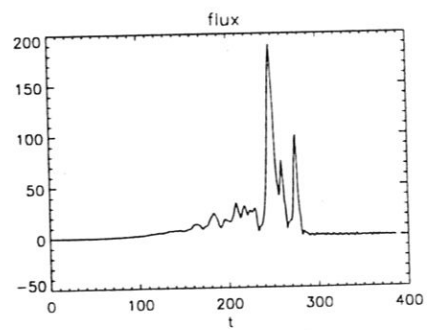
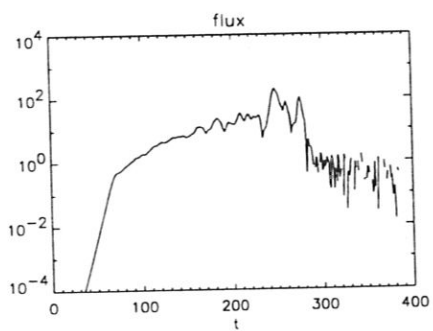
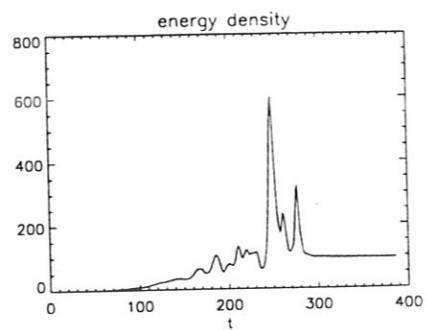
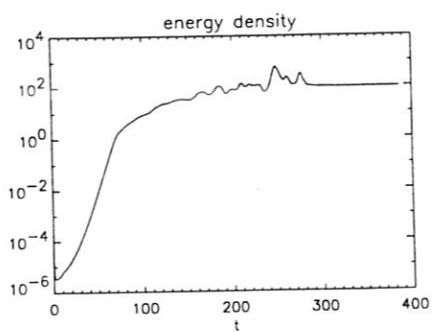
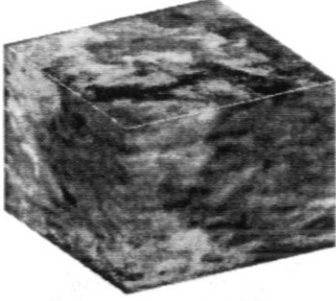
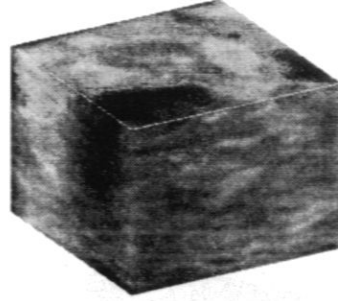


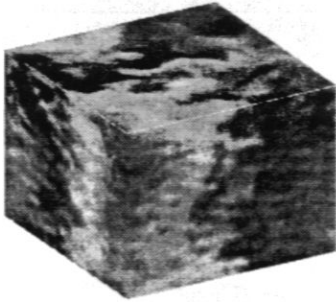
Figure 1: Time evolution of energy density and flux



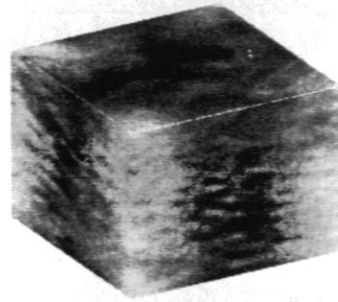
$t = 154, n$



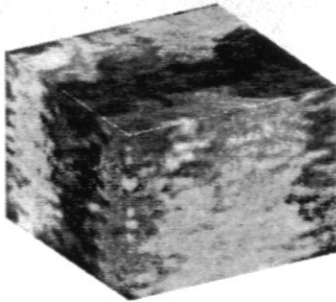
$t = 154, \phi$



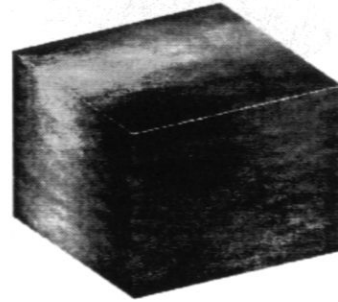
$t = 184, n$



$t = 184, \phi$

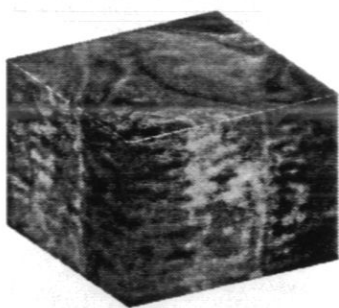


$t = 245, n$

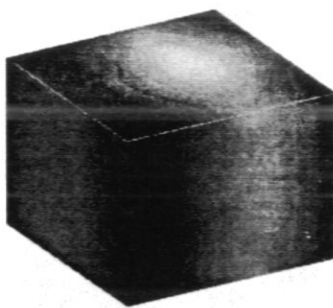


$t = 245, \phi$

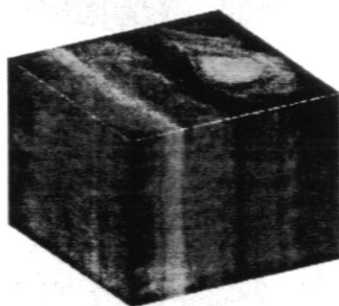
Figure 2: Evolution of n and ϕ : White corresponds to positive and black to negative density or potential, respectively. The magnetic field points into the vertical direction and the density profile increases towards the left.



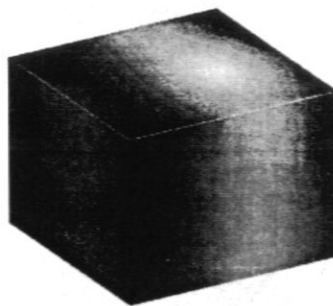
$t = 286, n$



$t = 286, \phi$



$t = 361, n$



$t = 361, \phi$

Figure 3: Continuation of Fig. 2

The observation that strong increases of the turbulent energy coincide with radial shear-flows suggests the following interpretation. The $k_z = 0$ modes of ϕ convect the density as a passiv scalar. This leads to an algebraic growth of $k_z = 0$ modes of n according to

$$\frac{\partial n}{\partial t} = -\frac{\partial \phi}{\partial y}, \quad (13)$$

where we have neglected the nonlinearity and the viscous damping. Since within the $k_z = 0$ modes there is no coupling from n to ϕ , the energy which is injected into the density must be transferred nonlinearly to $k_z \neq 0$ modes to allow a drive of the vorticity and hence to complete the nonlinear mechanism. Physically this may be understood as the growth of drift-wave eddies (due to the linear instability) located at the steep poloidal gradients of n which are generated from the radial profile by the radial shear flow. These drift-wave eddies tend to enhance the radial shear-flow by vortex-peeling (see ref. [8] and Fig. 4). An analytic model of this mechanism is derived in ref. [9], where it is also demonstrated that this nonlinear instability dominates the linear drive in the 3D Hasegawa-Wakatani model.

To confirm this model and to check the importance of the spectral transfer in k_z we measure the k_z -distribution of the different terms in the energy theorem

$$\frac{1}{2} \frac{d}{dt} \langle (\nabla_{\perp} \phi)^2 + n^2 \rangle = \langle \phi (\vec{v}_E \cdot \nabla_{\perp} \nabla_{\perp}^2 \phi) \rangle - \langle n (\vec{v}_E \cdot \nabla_{\perp} n) \rangle - \langle n \frac{\partial \phi}{\partial y} \rangle + \langle (\phi - n) \frac{\partial^2}{\partial z^2} (\phi - n) \rangle \quad (14)$$

with $\vec{v}_E = -\nabla_{\perp} \phi \times \vec{z}$ (the viscous terms have been dropped). The spatial averages correspond to a sum over all modes in Fourier-space:

$$\langle fg \rangle = \sum_{k_z} \sum_{\vec{k}_{\perp}} f_{\vec{k}_{\perp}, k_z}^* g_{\vec{k}_{\perp}, k_z}. \quad (15)$$

The total sum over k_z is zero for the two nonlinear contributions, but if the different k_z -modes are evaluated separately they measure the nonlinear source/sink rate in k_z . Hence we compute

$$\sum_{\vec{k}_{\perp}} f_{\vec{k}_{\perp}, k_z}^* g_{\vec{k}_{\perp}, k_z} + \sum_{\vec{k}_{\perp}} f_{\vec{k}_{\perp}, -k_z}^* g_{\vec{k}_{\perp}, -k_z}, \quad k_z \neq 0 \quad (16)$$

$$\sum_{\vec{k}_{\perp}} f_{\vec{k}_{\perp}, 0}^* g_{\vec{k}_{\perp}, 0}, \quad k_z = 0. \quad (17)$$

In Fig. 5 source/sink rates are plotted after averaging over several time slices between $t = 185$ and $t = 276$. In the source term $-n \partial \phi / \partial y$ the $k_z = 0$ modes play the dominante role (see plot (a)). The injected energy is transferred by the convective term to larger k_z modes where the coupling to ϕ takes place, mediated by the resistive term $\nabla_{\parallel}^2 (\phi - n)$ (see plot (b)). The convective term in the vorticity equation shifts the energy down to lower k_z . The total drive provided by the two terms is strongly localized at $k_z = 0$, where the radial shear flow mode is localized which causes the large source in $-n \partial \phi / \partial y$.

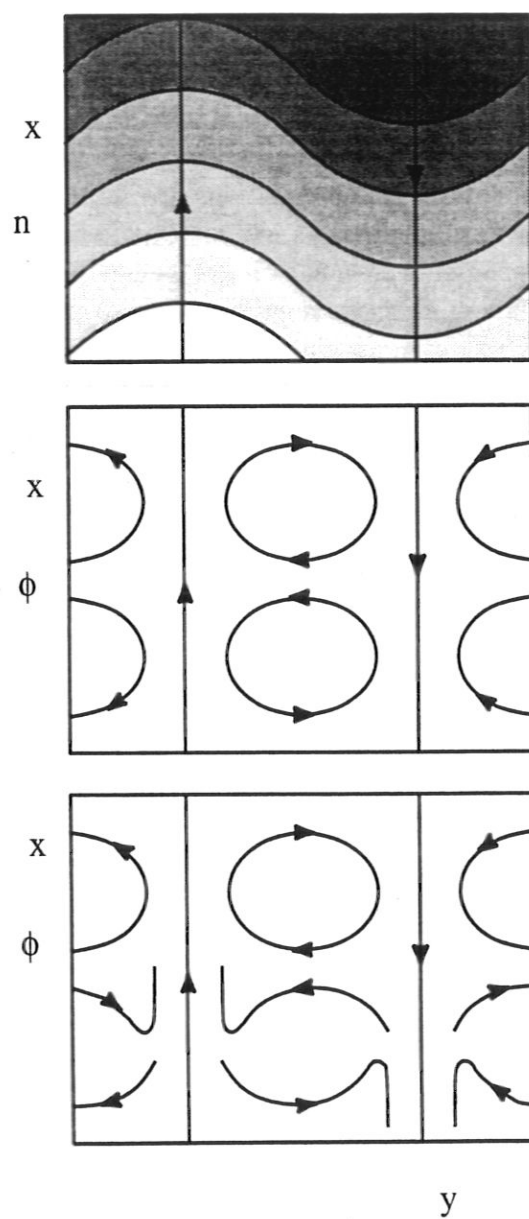


Figure 4: Schematic illustration of the nonlinear instability mechanism

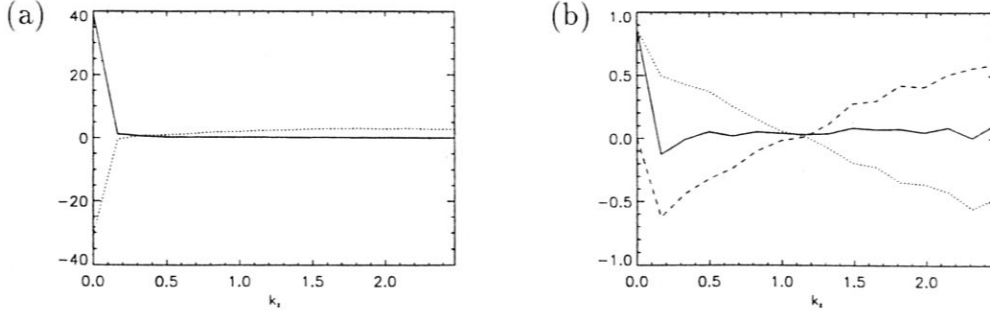


Figure 5: Energy source/sink spectra; (a): $-n\partial\phi/\partial y$ (solid line) and $-n(\vec{v}_E \cdot \nabla_{\perp} n)$ (dotted line); (b): $\phi(\vec{v}_E \cdot \nabla_{\perp} \nabla_{\perp}^2 \phi) + \phi \nabla_{\parallel}^2(\phi - n)$ (solid line), $\phi(\vec{v}_E \cdot \nabla_{\perp} \nabla_{\perp}^2 \phi)$ (dotted line) and $\phi \nabla_{\parallel}^2(\phi - n)$ (dashed line)

An important issue is the stability of the radial and poloidal shear flows (Kelvin-Helmholtz instability). The shear flows which we observe are always localized at the smallest k_x or k_y mode, respectively. In a computational box with periodic boundary conditions and $L_x = L_y$ both poloidal and radial shear flows are stable. If $L_y > L_x$ a poloidal shear flow is unstable and flips into the radial direction. In the same way a poloidal shear flow may be stabilized by $L_x > L_y$. To study this effect we perform a simulation with $L_y = 1.25 \cdot L_x$. The poloidal shear flow does not occur and hence the total energy in the system continues to grow without limit. This shows that the behavior of the unsheared 3D Hasegawa-Wakatani system is strongly affected by the box size, since there is no mechanism to stop the inverse cascade of the vorticity before it reaches the largest possible wavelength defined by the box size. This issue will be discussed further after studying the case with magnetic shear.

The last issue we want to discuss is the difference between the 3D and the 2D system. In the unsheared 2D system the nonlinear instability was never observed (in contrast to the sheared system [4] where a spectrum of k_{\parallel} modes is present). This becomes clear when eqn. (13) is translated into the 2D situation

$$\frac{\partial n}{\partial t} = -\frac{\partial \phi}{\partial y} + C(\phi - n). \quad (18)$$

The density is not only coupled to the radial velocity but via C also to the potential. In the same way ϕ is also coupled to the density by the parallel diffusion term. In this situation the algebraic growth observed in 3D does not occur. Hence the 2D system can not reproduce the behavior of the 3D system, where the transfer processes in the k_z spectrum play the dominant role.

5 Simulations with magnetic Shear

Magnetic shear not only stabilizes the linear instability in the Hasegawa-Wakatani system, but also has, combined with viscous damping, a major impact on the dissipation of large scale radial flows. An eddy with a large radial flow is not located on a single flux surface but extends over a finite radial domain. As the eddy spreads along the local magnetic field it becomes distorted since the orientation of the magnetic field varies with radial location. As a consequence an eddy which is radially extended at one location twists in the poloidal plane and becomes compressed in the radial direction and stretched in the poloidal direction as it maps down a field line. The resulting increase of the perpendicular gradients causes increased viscous damping. Mathematically this is implied in the explicit z -dependence of the ∇_{\perp}^2 -operator (eq. 7). As a consequence, the eddies become localized in parallel direction in contrast to the infinitely long eddies which are possible in the unsheared case. Hence we expect a strong influence of viscous damping on the generation of the radial flows which were responsible for driving the nonlinear instability in the unsheared system. Using a ∇_{\perp}^6 hyperviscosity as in the unsheared case the eddies are strongly damped only if gradients are very steep. In this case we expect radial convective cells to extend a long distance along the magnetic field. If we use ordinary viscosities $\mu \nabla_{\perp}^2$ as in ref. [6] with μ of realistic order of magnitude for ion-ion collisional damping, the eddies become damped even at moderate gradients. The Reynolds stress generation mechanism for the radial flows is also impacted by magnetic shear: the vortex-peeling mechanism [8] requires extended eddies which are oriented parallel to each other. This is possible if eddies are centered on the same flux surface and remain parallel as they map along the magnetic field. Hence poloidal shear flow which is generated by such an array of vortices can be generated relatively easily. In contrast, eddies which are stacked radially remain parallel only over a finite distance along the magnetic field. Hence the radial sheared flow which arises from such an array of vortices should be driven much more weakly than in the unsheared situation.

5.1 Comparison to the unsheared Case

Although most of our simulations with magnetic shear were performed with a more complete set of equations including the parallel ion velocity and with different damping operators, we first discuss a simulation very similar to the unsheared situation. We solve equations (5) and (6), but with the scaling $L_{\perp} = \rho_s$ (hence $\hat{\rho}_s \equiv 1$ and ∇_{\perp}^2 as in eq. (7)) discussed previously to facilitate the comparison with the unsheared case. We use the box dimensions $L_x = 22.9$, $L_y = 24.0$, $L_z = 26.8$, and the finite shear parameter $L_{\parallel}/L_s = 0.7$. The hyperviscosities were $\nu \nabla_{\perp}^8 \phi$ and $\nu \nabla_{\perp}^6 n$ with $\nu = 1.0 \times 10^{-4}$, and the resolution was 48×48 modes in the perpendicular plane and 96 grid points along the magnetic field (The computational domain is described in detail in ref. [6]).

As is well known, magnetic shear stabilizes the drift-wave system. Hence in order to study nonlinear effects we have to start from a state of sufficiently high

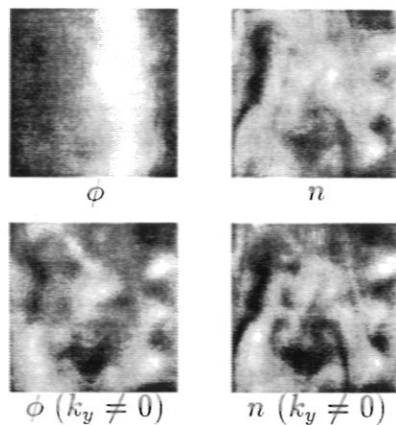


Figure 6: Poloidal cross-sections of ϕ and n at one location. In the lower plots the shear-flow modes $k_y = 0$ have been deleted.

amplitude. We choose a fully developed turbulent state generated by a resistive ballooning-instability (see refs. [5] and [6]). The most surprising result is the fact that the turbulence is driven nonlinearly (see refs. [9] and [6]). In the run we discuss here the turbulent energy remains at a level of 4.8 ± 0.8 and the average flux is 0.25 ± 0.07 . These levels are one to two orders of magnitude below the results in the unsheared run. As discussed previously, the Reynolds-stress induced formation of radial shear flows should be much weaker in a system with magnetic shear and we never observe a situation comparable to Fig. 2 at $t = 245$. The formation of poloidal shear flows is, however, possible since due to the localization of the viscous damping at high mode numbers eddies are only weakly damped. We observe during the whole run a moderate poloidal shear flow, which is clearly seen in Fig. 6. The stabilizing influence, however, seems to be very weak: the fluctuation-amplitudes are roughly the same as in a run discussed below with ∇_{\perp}^2 -type viscous damping where no poloidal shear flow was obtained. Nevertheless the transport in the current run is even 40% larger than in the simulation without shear flow. In the lower two plots of Fig. 6 potential and density are shown after removing the $k_y = 0$ shear-flow modes. Note the similarity between ϕ and n in contrast to the run without magnetic shear where the passively convected density showed a lot of fine-scale structure in the poloidal plane (Fig. 2). Contour plots of the perpendicular correlation functions of n and ϕ (Fig. 7) show that the size of the dominant structures is well separated from the box-size (this was checked also by a run with doubled box-size) in contrast to the unsheared situation where shear flows and eddies always tend to reach the system size. Finally Fig. 8 shows the energy source/sink spectra in k_z . Compared to Fig. 5 the source is spread over a larger range of modes, because the radial shear-flow at $k_z = 0$ does not occur in the situation with magnetic shear. The different

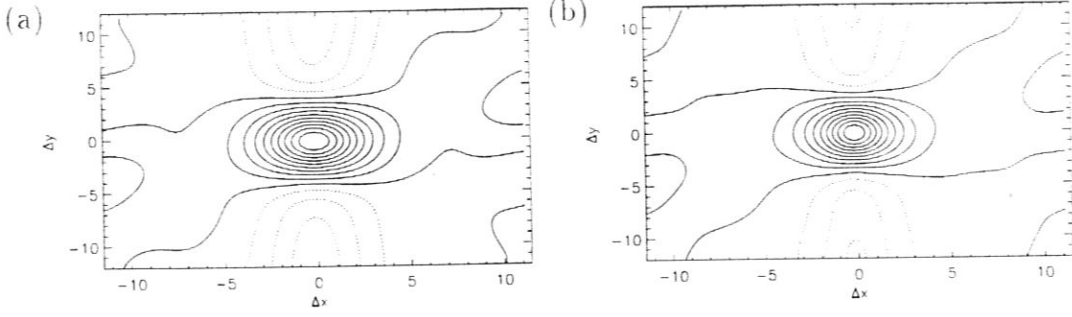


Figure 7: Autocorrelation function in the perpendicular plane after removing the $k_y = 0$ modes. (a) ϕ , (b) n

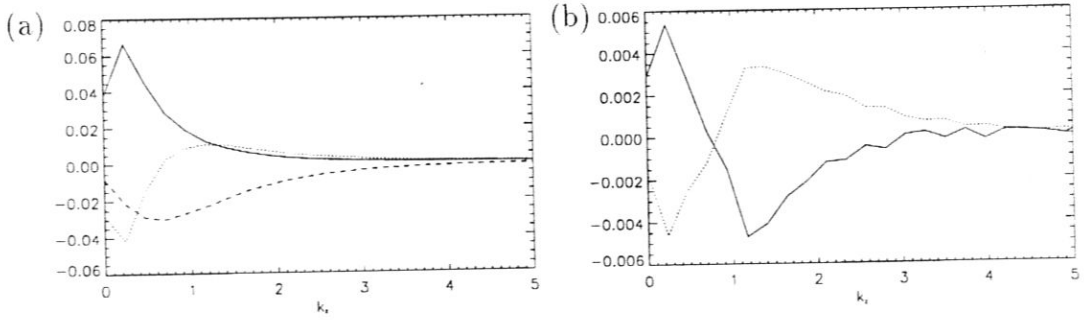


Figure 8: Energy source/sink spectra; (a): $-n\partial\phi/\partial y$ (solid line), $-n(\vec{v}_E \cdot \nabla_\perp n)$ (dotted line), and $-n\nabla_\parallel^2(\phi - n)$ (dashed line); (b): $\phi(\vec{v}_E \cdot \nabla_\perp \nabla_\perp^2 \phi)$ (solid line), and $\phi\nabla_\parallel^2(\phi - n)$ (dotted line). Since the computational domain is not periodic in z , the values for $k_z = 0$ may be non-zero also for the ∇_\parallel term.

magnitude of the source/sink spectra reflects the lower overall energy and transport level of the current simulation. The energy injected into n cascades partially to larger k_z , partially it is dissipated by the parallel diffusion term and transferred into ϕ at the same k_z at which it is injected. For the potential the situation is quite similar to Fig. 5. The resistive term drives the system at high k_z in a mode number range which contributes little to the drive term $-n\partial\phi/\partial y$. The energy cascades to low k_z modes corresponding to the usual inverse cascade. There it is damped by the parallel resistive term, but nevertheless the kinetic energy in this low k_z mode range causes the drive of the system as shown by the plot of $-n\partial\phi/\partial y$. The energy flow in general shows that despite the absence of large scale radial shear-flows the nonlinear drive mechanism is basically the same as in the unsheared case.

In summary the simulation with magnetic shear shows the dominance of the nonlinear mechanism which is able to maintain the linearly stable system in a turbulent state. On the other hand the results also indicate very clearly that although the drive mechanism is the same, it is impossible to predict the properties of the sheared system based on simulations without magnetic shear. Unlike in the unsheared system, the Kelvin-Helmholtz stability of the largest scale radial flows does not control the dynamics of the sheared system because of the computational domain in the twisted coordinates (see ref. [6]). In the unsheared system with $L_y > L_x$, the radial flow of the lowest order k_y convective cell is Kelvin-Helmholtz stable and there is therefore no saturation of the nonlinear instability. With magnetic shear such a long wavelength radial flow is only oriented in the radial direction at a single value of z . As the disturbance projects along \vec{B} , it twists in the poloidal plane, becoming squashed in the radial direction and stretched in the poloidal direction. In this region the flow is now locally Kelvin-Helmholtz unstable and can cause the breakup of the flow. The singular behavior of the unsheared system is therefore absent.

5.2 Influence of the Parameter $\hat{\rho}_s$

We now explore the influence of $\hat{\rho}_s$ on the turbulence and transport (using the original scaling of eqs. (5) and (6)). For this parameter scan we used a more general set of equations which include the parallel ion velocity (see also refs. [5] and [6]; since the computations are very expensive, we did not repeat them without the parallel velocity.)

$$\frac{d}{dt}\nabla_{\perp}^2\phi + \frac{\partial^2}{\partial z^2}(\phi - n) = D^{\phi}, \quad (19)$$

$$\frac{dn}{dt} + \frac{\partial\phi}{\partial y} + \hat{\rho}_s^2 \frac{\partial^2}{\partial z^2}(\phi - n) + \gamma \frac{\partial v_{\parallel}}{\partial z} = D^n, \quad (20)$$

$$\frac{dv_{\parallel}}{dt} + \gamma \frac{\partial n}{\partial z} = D^{v_{\parallel}}, \quad (21)$$

where $\gamma = L_n/(2\pi L_s \hat{\rho}_s)$ is the normalized sound speed. In the dissipation terms we use ordinary diffusion operators $\nu \nabla_{\perp}^2$ and the parallel damping $\kappa \nabla_{\parallel}^2$ with $\nu = 1.5 \times 10^{-3}$ and $\kappa = 1.0 \times 10^{-3}$.

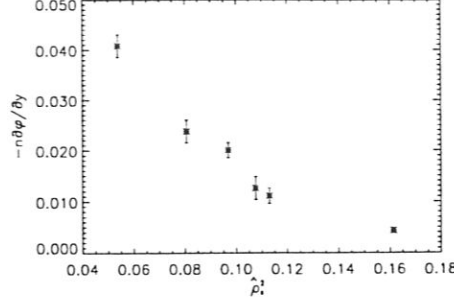


Figure 9: Flux $-n\partial\phi/\partial y$ versus $\hat{\rho}_s^2$. For $\hat{\rho}_s^2 = 0.162$ the nonlinear drive is very weak and the turbulence eventually died away.

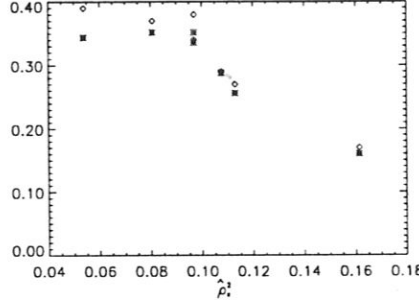


Figure 10: Fluctuation amplitude versus $\hat{\rho}_s^2$: $\langle\phi^2\rangle^{1/2}$ (stars) and $\langle n^2\rangle^{1/2}$ (diamonds)

We performed several simulations with $\hat{\rho}_s^2$ ranging from 0.054 to 0.162. The box dimensions were $L_x = 5.3$, $L_y = 5.6$, $L_z = 3.0$ with 48×48 modes in the perpendicular plane and 96 collocation points along z . To check if the eddy-size is influenced by the box-size we also performed runs with doubled box-size in the perpendicular plane and obtained essentially the same results as in the present system. According to the mechanism discussed in the unsheared case, we expect the strongest nonlinear drive if n is convected by the $\vec{E} \times \vec{B}$ -velocity without constraints. Since the $\hat{\rho}_s^2$ -term in the continuity equation (6) interferes with this free convection, the efficiency of the nonlinear mechanism should be reduced by increasing $\hat{\rho}_s$. This is exactly observed in the simulations: increasing $\hat{\rho}_s^2$ by a factor of 2 reduces the transport by a factor of 4 (Fig. 9). The same tendency is found for the fluctuation amplitudes (Fig. 10) where a decay of a factor of 2 is in perfect agreement to the reduction of the flux by a factor of 4. To investigate this drop of the turbulence and the approach to a stable situation in more detail we check the energy transfer (Fig.

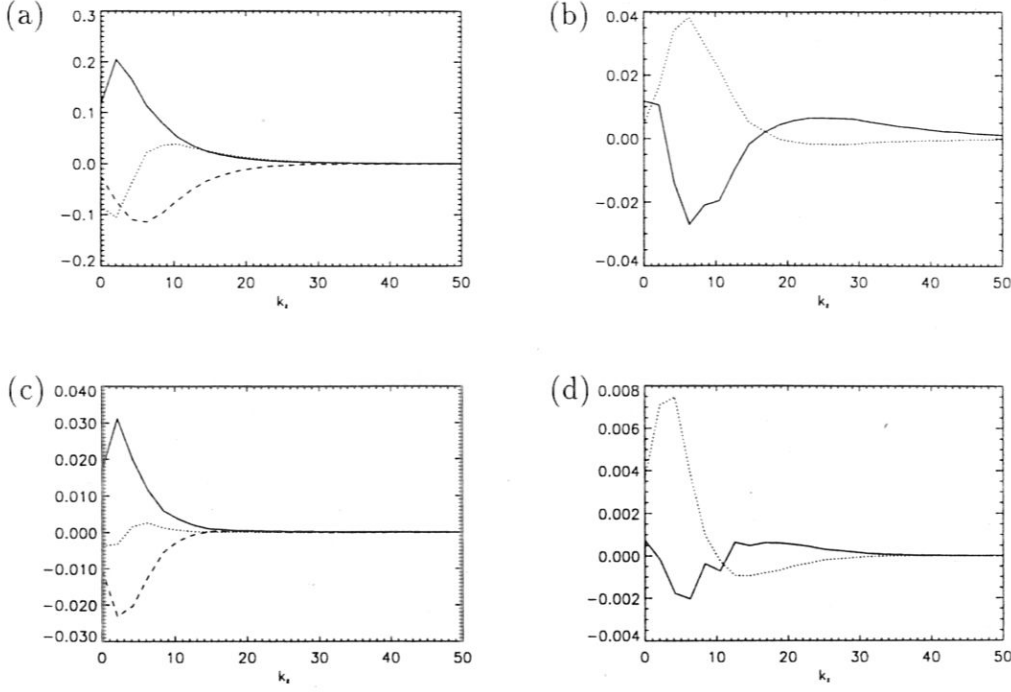


Figure 11: Energy source/sink spectra, (a,b): $\hat{\rho}_s^2 = 0.054$, (c,d) $\hat{\rho}_s^2 = 0.162$; (a,c): $-\hat{\rho}_s^{-2}n\partial\phi/\partial y$ (solid line), $-\hat{\rho}_s^{-2}n(\vec{v}_E \cdot \nabla_\perp n)$ (dotted line), and $-n\nabla_\parallel^2(\phi - n)$ (dashed line); (b,d): $\phi(\vec{v}_E \cdot \nabla_\perp \nabla_\perp^2 \phi)$ (solid line), and $\phi\nabla_\parallel^2(\phi - n)$ (dotted line). Since the computational domain is not periodic in z , the terms proportional to ∇_\parallel^2 may be non-zero at $k_z = 0$.

11). For $\hat{\rho}_s^2 = 0.054$ approximately half of the energy injected into the density-fluctuations is transferred nonlinearly to higher k_z , which leads to a peaking of the resistive sink at significantly higher mode-numbers. Correspondingly the resistive source in the vorticity equation is located at moderately high k_z and requires a nonlinear transfer to the low- k_z eddies. If $\hat{\rho}_s^2$ is increased to 0.162 this picture changes significantly. The nonlinear transfer in the continuity equation becomes negligible. Hence almost all fluctuation energy is dissipated at the same scale where it is injected. The same result is found in the vorticity equation: the nonlinear transfer is negligible compared to the resistive drive. Since except for $k_z = 0$ all nonlinear interactions between different perpendicular modes are associated with a nonlinear interaction in k_z , the negligible energy transfer in k_z is equivalent to a negligible overall nonlinear interaction including any flow enhancement by Reynolds-stress. The observed stabilization of the system is caused by the relative reduction of the nonlinear terms compared to the linear terms. The fluctuation-amplitude becomes sufficiently low for $\hat{\rho}_s^2 \approx 0.15$ that the nonlinear interaction is negligible

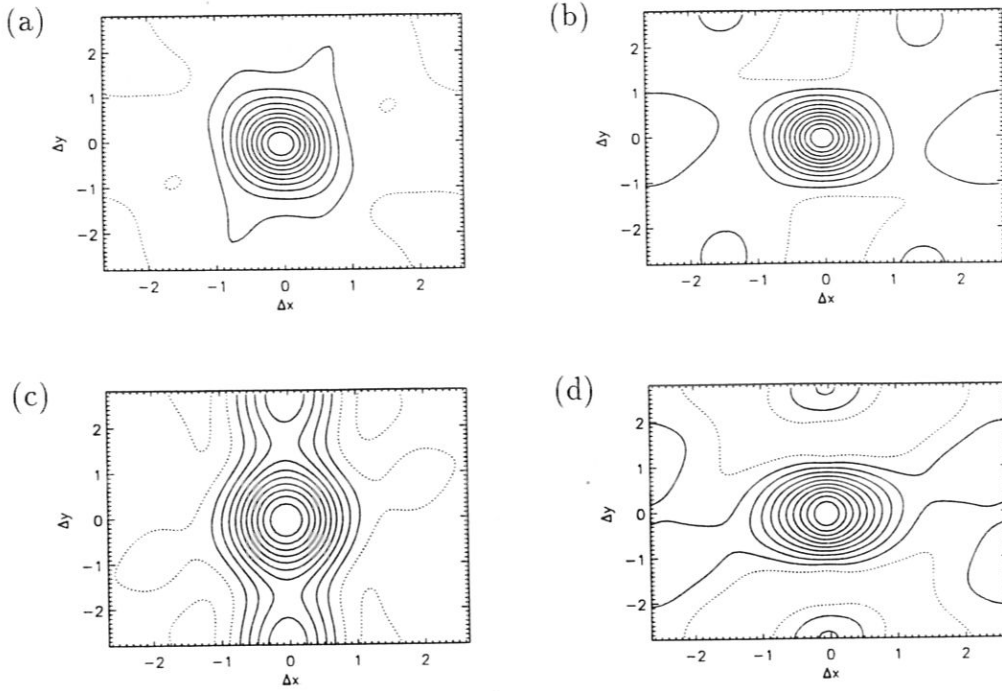


Figure 12: Autocorrelation function in the perpendicular plane; $\hat{\rho}_s^2 = 0.054$: (a) ϕ , (b) n ; $\hat{\rho}_s^2 = 0.162$: (c) ϕ , (d) n

and the system is stabilized as described by a linear analysis of the equations.

The last issue is the intrinsic size of the turbulence in the perpendicular plane: do the eddies scale with $\hat{\rho}_s$ and therefore vary in size as $\hat{\rho}_s$ is changed or is their transverse scale controlled by the magnetic shear as given in (4) and therefore remain fixed in size as $\hat{\rho}_s$ is changed. As is seen in Fig. 12 the perpendicular scale length is unchanged although $\hat{\rho}_s^2$ is increased by a factor of 3. Thus, magnetic shear and not $\hat{\rho}_s$ controls the transverse scale of the turbulence. The correlation length in the parallel direction is increased with larger $\hat{\rho}_s$ (Fig. 13). This reflects the fact that $\hat{\rho}_s^2$ plays the role of a parallel diffusion in the continuity equation (6). It affects in particular the small k_z drift waves, hence an increase of $\hat{\rho}_s$ leads to a reduction of the nonlinear drive.

6 Conclusions

The most important feature of the 3D drift-wave system is its nonlinear drive, which is tightly coupled to a nonlinear interaction between different k_z -modes. This leads to a behavior of the 3D Hasegawa-Wakatani system, which is completely differ-

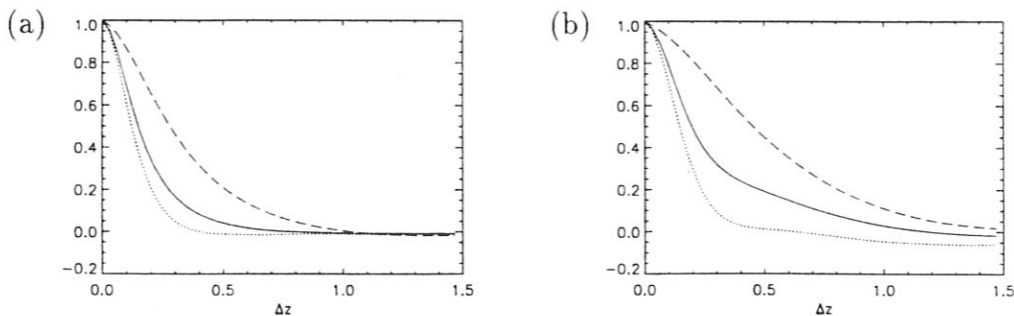


Figure 13: Autocorrelation function in parallel direction: (a) $\hat{\rho}_s^2 = 0.054$, (b) $\hat{\rho}_s^2 = 0.162$; n (solid line), ϕ (dotted line), and $\phi - n$ (dashed line)

ent from predictions based on 2D simulations. The radial shear-flows in the un-sheared simulations lead to transport bursts with an anomalous diffusion rate of $D_{an} = 10^2 \times D_{GB}$ being orders of magnitude larger than observed in experiment. This feature of the unsheared system may be attributed to the lack of a mechanism which could stop the inverse cascade of the kinetic energy and keep the turbulent eddies from reaching the box size. As a consequence poloidal or radial shear flows are formed at the lowest possible k . The stability of these shear flows to a Kelvin-Helmholtz mechanism is tightly coupled to the box dimensions and the boundary conditions applied. Hence the behavior of the system strongly depends on artificial box size effects. Including magnetic shear into the equations solves this problem. The alignment of the turbulent eddies along \vec{B} requires a different orientation at different flux surfaces and leads to a limitation of the eddy size. Equivalently the different orientation of the eddies at different radial location weakens the Reynolds stress-induced generation of radial shear-flows. As a consequence the simulations show a stationary nonlinearly driven turbulent state, where the size of the dominant structures is independent on the box size. The resulting transport is of the experimentally observed magnitude (see ref. [6]). Changing the remaining free parameter $\hat{\rho}_s^2$ has a strong impact on the turbulence level and at sufficiently large values stabilizes the nonlinear drive by reducing the fluctuation amplitudes and hence the strength of the nonlinear interaction compared to the linear dissipation terms.

References

- [1] A. Hasegawa, M. Wakatani, Phys. Rev. Lett. **50**, 682 (1983).
- [2] A. E. Koniges, J. A. Crotinger, and P. H. Diamond, Phys. Fluids B **4**, 2785 (1992).

- [3] S. J. Camargo, D. Biskamp, and B. D. Scott, *Phys. Plasmas* **2**, 48 (1995).
- [4] B. D. Scott, H. Biglari, P. W. Terry, and P. H. Diamond, *Phys. Fluids B* **3**, 51 (1991).
- [5] P. N. Guzdar, J. F. Drake, D. C. McCarthy, A. B. Hassam, and C. S. Liu, *Phys. Fluids B* **5**, 3712 (1993).
- [6] A. Zeiler, J. F. Drake, D. Biskamp, and P. N. Guzdar, submitted 1995.
- [7] D. Biskamp, A. Zeiler, *Phys. Rev. Lett.* **74**, 706 (1995).
- [8] J. F. Drake, J. Finn, P. Guzdar, V. Shapiro, V. Shevchenko, F. Waelbroeck, A. B. Hassam, C. S. Liu, and R. Z. Sagdeev, *Phys. Fluids B* **4**, 488 (1992).
- [9] J. F. Drake, A. Zeiler, and D. Biskamp, *Phys. Rev. Lett.* **75**, 4222 (1995).